

Comparison of aerosol backscatter and wind field estimates from the REAL and the SAMPLE

Shane D. Mayor^a, Pierre Dérian^a, Christopher F. Mauzey^a, Scott M. Spuler^b,
Patrick Ponsardin^c, Jeff Pruitt^c, Darrell Ramsey^c, and Noah S. Higdon^c

^aCalifornia State University Chico, Chico, California, USA;

^bNational Center for Atmospheric Research, Boulder, Colorado, USA;

^cSpectral Sensor Solutions, LLC, Herndon, Virginia, USA

ABSTRACT

Although operating at the same near-infrared 1.5- μm wavelength, the Raman-shifted Eye-safe Aerosol Lidar (REAL) and the Scanning Aerosol Micro-Pulse Lidar—Eye-safe (SAMPLE) are very different in how they generate and detect laser radiation. We present results from an experiment where the REAL and the SAMPLE were operated side-by-side in Chico, California, in March of 2015. During the non-continuous, eleven day test period, the SAMPLE instrument was operated at maximum pulse repetition frequency (15 kHz) and integrated over the interpulse period of the REAL (0.1 s). Operation at the high pulse repetition frequency resulted in second trip echoes which contaminated portions of the data. The performance of the SAMPLE instrument varied with background brightness—as expected with a photon counting receiver—yet showed equal or larger backscatter intensity signal to noise ratio throughout the intercomparison experiment. We show that a modest low-pass filter or smooth applied to the REAL raw waveforms (that have 5x higher range resolution) results in significant increases in raw signal-to-noise ratio and image signal-to-noise ratio—a measure of coherent aerosol feature content in the images resulting from the scans. Examples of wind fields and time series of wind estimates from both systems are presented. We conclude by reviewing the advantages and disadvantages of each system and sketch a plan for future research and development activities to optimize the design of future systems.

Keywords: lidar, aerosol, wind, atmosphere, eyesafe lidar, elastic backscatter lidar

1. INTRODUCTION

Detection subsystems in atmospheric lidars can be divided into two broad categories: heterodyne detection and direct detection. Heterodyne detection is employed to measure minute frequency shifts of coherent backscattered radiation in order to determine the radial component of wind velocity. Direct detection is employed in the majority of other lidar systems, and including some non-heterodyne Doppler lidars. Within the category of direct-detection, there are two possible choices: analog detection and photon counting. Analog detection systems are used when the rate of arrival of backscatter photons is too large to be counted individually. They use detectors such as avalanche photodiodes (APDs) and transimpedance amplifiers to convert a flux of photons on the active area of the detector to a voltage that can be recorded by an analog to digital converter.

Photon counting detection subsystems can be used when the photon arrival rate is lower than approximately 10M s^{-1} . Photon counting subsystems (also known as Geiger-mode detection subsystems) may also be referred to as digital direct detection. Some lidar systems split the backscattered radiation into both an analog detection and photon counting subsystems.¹ In such lidars, the analog data are used when the backscatter signal intensity is large and the photon counting data are used when the intensity is weak. Photomultiplier tubes (PMTs) and single-photon avalanche diodes (SPADs) are used in photon counting systems.^{2,3}

So, the choice of whether to use analog or digital detection depends on the return signal intensity, which largely depends on the transmitter pulse energy. Strong transmit pulse energy generally results in strong backscatter

Further author information:

S.D.M.: E-mail: sdmayor@csuchico.edu, Telephone: 1 530 898 6337

N.S.H.: E-mail: scott.higdon@s-3llc.com, Telephone: 1 703 608 2325

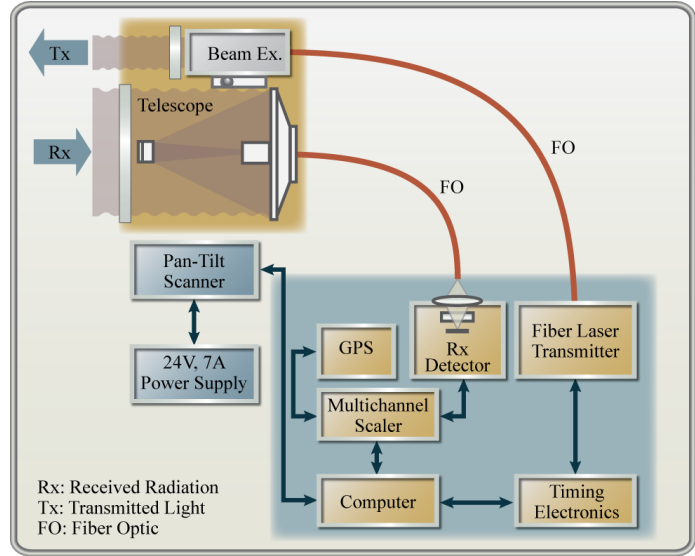


Figure 1: Left panel: Photograph of the SAMPLE (Summer of 2015). Right panel: General schematic of the SAMPLE.

intensity, high photon arrival rate, and requires analog detection. Weak transmit pulse energy results in weak backscatter intensity, low photon arrival rate, and requires photon counting. Because of this general division, we refer to systems employing large pulse energy and analog detection as “macropulse” and systems employing weak pulse energy and photon counting as “micropulse”. Indeed, micropulse lidars often transmit with pulse energy on the order of tens to hundreds of microjoules.⁴

A well-designed macropulse lidar has the advantage of receiving all the backscattered radiation necessary to observe atmospheric structure over a long path (typically a few kilometers in the horizontal direction) from a single pulse. This leads to the advantages of being able to scan rapidly and acquire data with high angular resolution without having to integrate data from multiple pulses. However, macropulse lidars require lasers capable of large pulse energy. Such lasers tend to be bulk lasers with wavelength converters. Free space optics are required to handle the beam in the transmitter. Because the pulse energy is large and the beam handling optics are small (order 1 inch diameter or less), the energy density in the transmitter may be very large. This results in the relatively large physical sizes of such devices. Finally, such transmitters are notorious for being expensive, sensitive to environmental conditions, and requiring high levels of care and maintenance.

Micropulse lidars have the advantages of employing waveguide lasers that produce low pulse energy. These lasers tend to be less expensive, more compact, and all-solid state. They are more rugged, require no liquid cooling, and use less free-space optics (i.e., more fiber-based components) and, as such, are less sensitive to environmental conditions. On the other hand, because the backscatter signal is so small from each pulse, micropulse lidars require the integration of backscatter intensity over many pulses (under most conditions, the signal-to-noise ratio improves by the square root of the number of pulses in the integration period.) Furthermore, two additional disadvantages appear: First, because the detection systems are so sensitive, background radiation becomes a significant source of noise and requires careful filtering. Second: practical limitations in pulse rate begin to appear from second trip echoes. That is while any given pulse is traversing the region of primary interest (the first few kilometers range), backscatter signal from distant clouds or hard targets from previous pulses are superimposed on and confound the signal from the most recent pulse.

2. REAL

The original NSF Raman-shifted Eye-safe Aerosol Lidar (REAL)⁵⁻⁸ at California State University Chico provides high signal-to-noise ratio elastic backscatter to several kilometers range from individual laser pulses. The REAL pulse energy varies slowly over time ($\pm 20\%$) and depends mostly on the age of the flashlamps and the flashlamp

voltage—and to a lesser degree room temperature. During normal operation we strive to operate between 120 and 170 mJ/pulse. The transmitted pulse energy is strongly dependent on the wavelength conversion efficiency in the Raman shifter, which depends strongly on the fluence of the Nd:YAG pump beam. The pulse repetition frequency is 10 Hz. REALs built by ITT Corp. operate at 20 Hz.⁹ No integration of backscatter signal from multiple pulses in time is required to observe atmospheric structure over a long path. The REAL pulse duration is approximately 6 ns (corresponding to 1.8 m in length) and the receiver subsystem employs a 14-bit analog to digital converter operating at 100 MSPS. That results in a data point every 1.5 m in range. The combined bandwidth of the Perkin Elmer InGaAs APD (with detector active area of 200- μ m diameter) and amplifier electronics is about 10-20 MHz (corresponding to scales of 15 to 7.5 m in range.) The backscattered radiation is split into two channels on the original NSF REAL for relative polarization sensitivity.⁷ The REAL has resulted in impressive aerosol imagery that can be used with motion estimation algorithms to deduce vector wind fields.^{10–12} The REAL transmitter, however, is large and challenging to maintain. It places a very significant limitation on the embodiment of the entire instrument, sets substantial requirements for maintenance, and therefore reduces deployment opportunities.

3. SAMPLE

The Scanning Aerosol Micro-Pulse Lidar—Eye-safe (SAMPLE), shown in the left panel of Fig. 1 and on the left in Fig. 2 and available through Spectral Sensor Solutions LLC, integrates a combination of commercial-off-the-shelf and custom components into a compact system. A general system schematic is shown in the right panel of Fig. 1. The laser in the SAMPLE is a Keopsys erbium fiber laser Model KPS-BT2-PEYFA-1555-05-Col operating at approximately the same 1.5 micron wavelength as the REAL. The laser pulse energy is 300-500 times lower than that of the REAL, but the pulse repetition frequency is 1500 times higher. As a result, the SAMPLE transmits an average power of 5.25 W while the REAL transmits 1.2 - 1.7 W. The Keopsys laser is attached to a custom beam expander that increases the beam diameter to 10 cm for transmission into the atmosphere.

The SAMPLE receiver employs a custom 20-cm diameter telescope that is fiber-coupled to a Hamamatsu H10330-75 photon counting photo multiplier tube (PMT) with an active area that is 1.6 mm in diameter (64 times larger area than the APD used in the REAL). The photon count data are sampled at 20 MHz thereby providing backscatter intensity every 7.5 m in range. The multichannel scaler card is an Ortex model 9353.

Recently, the SAMPLE was upgraded to include a server with the same general purpose graphical processing units (GPUs) and motion estimation algorithms that are used by the REAL. This gives the system the same real-time 2D vector wind field sensing capability as the REAL. Properties of the REAL and the SAMPLE lidars are listed for comparison in Table 1.

4. EXPERIMENT

The SAMPLE was deployed in Chico, California, from 9–20 March 2015. The instrument was deployed from a U-Haul moving truck. Figure 2 is a photograph of both systems during operation. The beam steering unit of the REAL and the telescope of the SAMPLE were separated by approximately 10 m distance. The altitude of the site is 53 m ASL. Data were collected primarily during the day and early evening. No deliberate sources of particulate matter were created for the tests. The weather and aerosol conditions varied greatly during the 11 day experiment. The site is located in an active agricultural region with large orchards and other crops. The REAL operated continuously and the SAMPLE was operated for at least a few hours of every day of the 11 day experiment. The vast majority of scans collected were nearly-horizontal plan-position-indicator (PPI) scans at an elevation angle of 2° above the horizon. This was done because a major objective of the program was to test the horizontal wind component estimation capability described in section 7. Unfortunately, the SAMPLE at this time was not programmed to rapidly return the pan/tilt positioner (often referred to as the scanner) to the beginning azimuth angle after the completion of each scan (an action often referred to as “fly-back”). Instead, the subsequent scan was collected in the reverse scan direction. The impact of this is uneven temporal sampling of given point in the scan area. It makes the movement of features in the animations appear to “walk” rather than move fluidly. This issue has no impact on our ability to compare and analyze the signal to noise ratio performance of the SAMPLE with the REAL, but it does limit our ability to make fair wind field estimates resulting from the two systems.

Table 1: Comparison of system specifications for the REAL and the SAMPLE.

	Original NSF REAL	SAMPLE
Wavelength (microns)	1.543	1.554
Pulse rate (Hz)	10	15,000
Pulse energy (mJ)	120 - 170	0.35
Average transmit power (W)	1.2 - 1.7	5.25
Pulse duration (ns)	6	25
Pulse length (m)	1.8	7.5
Backscatter sample rate (MSPS)	100	20
Range gate spacing (m)	1.5	7.5
Transmitter type	Flashlamp-pumped Nd:YAG & Raman wavelength shifter	Pulsed fiber
Transmitter	Continuum Surelite III and custom Raman cell with CH ₄	Keopsys erbium fiber laser KPS-BT2-PEYFA-1555-05-Col
Beam divergence (mrad, half angle)	0.20	0.30
Optical filter bandwidth (nm)	5	1
Detection type	Analog InGaAs APD	Photon counting PMT
Detector brand & model	Perkin Elmer C30659-1550-R2A	Hamamatsu H10330-75
Detector active area diameter (mm)	0.2	1.6
Detector quantum efficiency (%)	75	12
Telescope diameter (cm)	40	20
Receiver FOV (mrad, half angle)	0.28	0.4
Geometry	coaxial	biaxial
Scan mechanism	beam steering unit	pan/tilt positioner



Figure 2: The SAMPLE on the left and the REAL on the right during a side-by-side comparison experiment on 9 March 2015 in Chico, California.

Figure 3 shows one PPI scan from the REAL (on left) and one PPI scan from the SAMPLE (on right). The data in Fig. 3 are of relative backscatter intensity in decibels. These scans were collected at the same time during evening twilight. At that time, a shallow temperature inversion was likely to have recently started forming very near the surface with neutral stability above. Winds were from the northwest. The backscatter fields shown in Fig. 3 were computed by standard lidar processing procedures such as computing and subtracting the mean

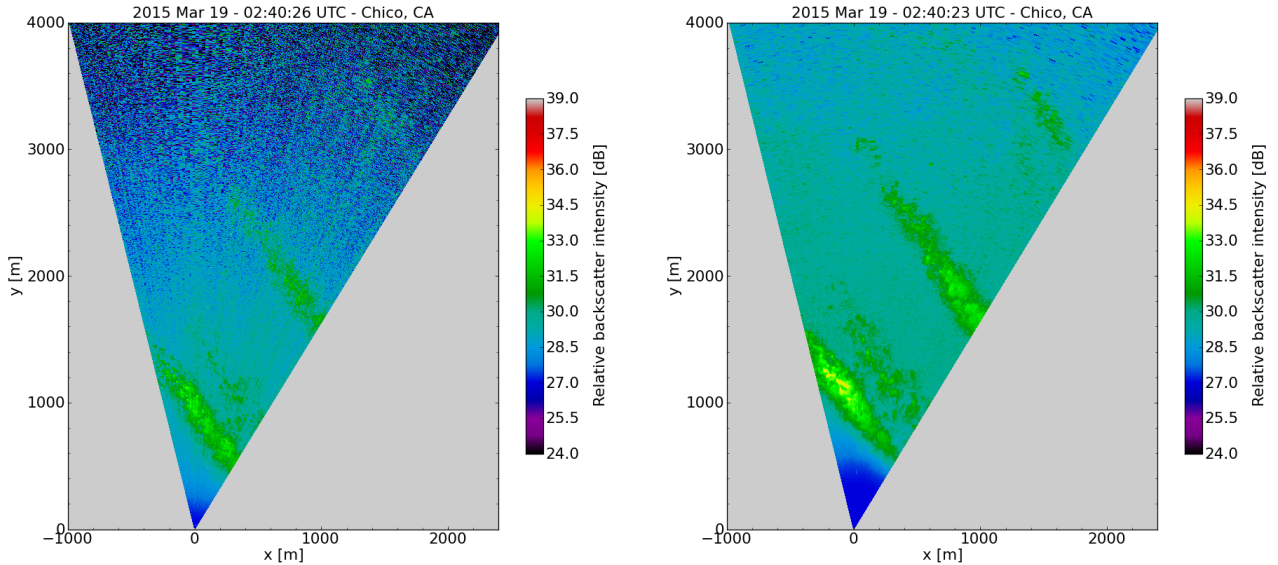


Figure 3: Left panel: one unfiltered PPI scan of relative aerosol backscatter intensity from the REAL. Right panel: the same from the SAMPLE.

background from every record in each scan, correcting for the inverse-square law, and converting to decibels. Effects of extinction are not corrected. The images show three aerosol plumes that are moving across the sector area. They are moving from the NW to the SE. We do not know the specific source of these plumes, but they are likely the result of agricultural activities such as the operation of heavy equipment. The images are very similar. However, differences include the appearance of stronger signal at far ranges in the SAMPLE image, more fine-scale detail at close ranges in the REAL image, and radial streaks in the REAL image that are associated with pulse to pulse variations in transmitted laser energy.

Figure 4 shows raw backscatter intensity as a function of range resulting from one pulse of the REAL and the closest possible 0.1 s integration of SAMPLE backscatter photon counts. These arrays came from the same scans as shown in Fig. 3 (at approximately 20° azimuth). Several significant characteristics can be noted. First, it is clear that the REAL detector was not optimally placed at the focus of the backscattered radiation, particularly in the along-axis (z) dimension. This means the overlap function is less than 1 at long ranges (the detector is not collecting all of the transmitted beam at longer ranges). It was not terribly off, but it explains why the REAL has much higher signal at the near ranges and why the roll-off, or decay, in scattering intensity is steeper than SAMPLE. Second, the REAL waveform (blue) exhibits larger amplitude high-frequency random noise. The main sources of this noise come from the excess noise factor of the APD and from the amplifier. Third, the region between 0 m and 600 m is where the transmitted laser beam and the receiver field of view are not completely overlapped. This comes from defocused receiver light overfilling the detector (which acts as the field stop) in the REAL and the biaxial geometry of the SAMPLE.

5. COMPARISON OF RAW SNR

Raw signal-to-noise (SNR) is the SNR of the backscatter intensity data before any processing is performed. Raw SNR is computed by dividing the backscatter signal amplitude $I_0(r, \theta)$ at each gate in range by the standard deviation of the backscatter background σ_θ for that radial array. Here, r is range and θ is the angle. The background is simply a subset of data points from the waveforms shown in Fig. 4 that are representative of incident power on the detector when backscatter is not present. The safest place to compute statistics of the background is from a set of data points just prior to the laser discharge (0 m range). Alternatively, data points

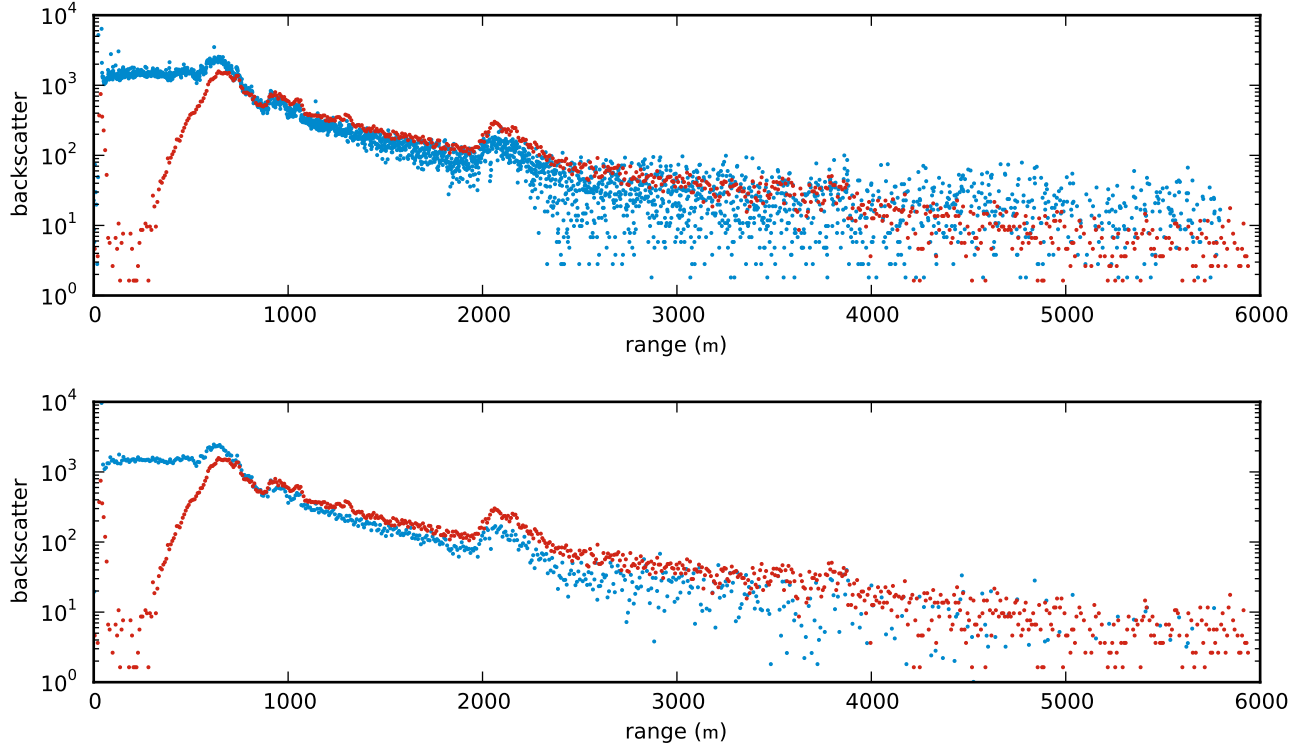


Figure 4: Raw backscatter waveforms from the REAL and SAMPLE after subtraction of background mean. The REAL waveform (blue) resulted from one laser pulse. The SAMPLE waveform (red) resulted from the integration of 1500 laser pulses during a 0.1 s interval. Top panel is with the native REAL resolution (1.5 m range gate), bottom panel with a 5-point binning to match SAMPLE resolution.

near the long-range end of the waveform (e.g., to the right of 5000 m in Fig. 4) may be used if they are clear of backscatter signal from aerosol, clouds, and hard targets. We note that $I_0(r, \theta)$ is the backscatter waveform after the mean background has been subtracted.

$$SNR_{raw}(r, \theta) = \frac{I_0(r, \theta)}{\sigma_\theta}. \quad (1)$$

Figure 5 shows the results of the calculation for the pair of waveforms shown in Fig. 4. Comparisons such as the one shown in Figs. 4 and 5 were performed for a variety of pointing angles and background conditions, although not shown here for brevity. The most impressive result was when the raw SNR of the SAMPLE was 6 – 10 times larger than that of the REAL during twilight conditions such as those shown. By binning the REAL data, the raw SNR of the SAMPLE was still 3 – 6 times larger than that of the REAL during those conditions. However, as the background radiation intensity increased the SAMPLE raw SNR decreased. For example, while scanning toward the north at noon, the SAMPLE raw SNR was only 1 – 2 times larger than that of the REAL. Binning the REAL data from the noon comparison resulted in slightly higher SNR for the REAL. We hypothesize that the background level depends on the position of the sun, the pointing direction of the lidar, and the presence and position of clouds and particulate matter that may scatter and absorb solar radiation. A comprehensive analysis of the raw SNR as a function of background level has not yet been performed.

6. COMPARISON OF IMAGE SNR

A goal of our work is to estimate 2-component vector wind fields and aerosol plume motion using motion estimation algorithms. A critical step for motion estimation is high-pass median filtering in order to remove

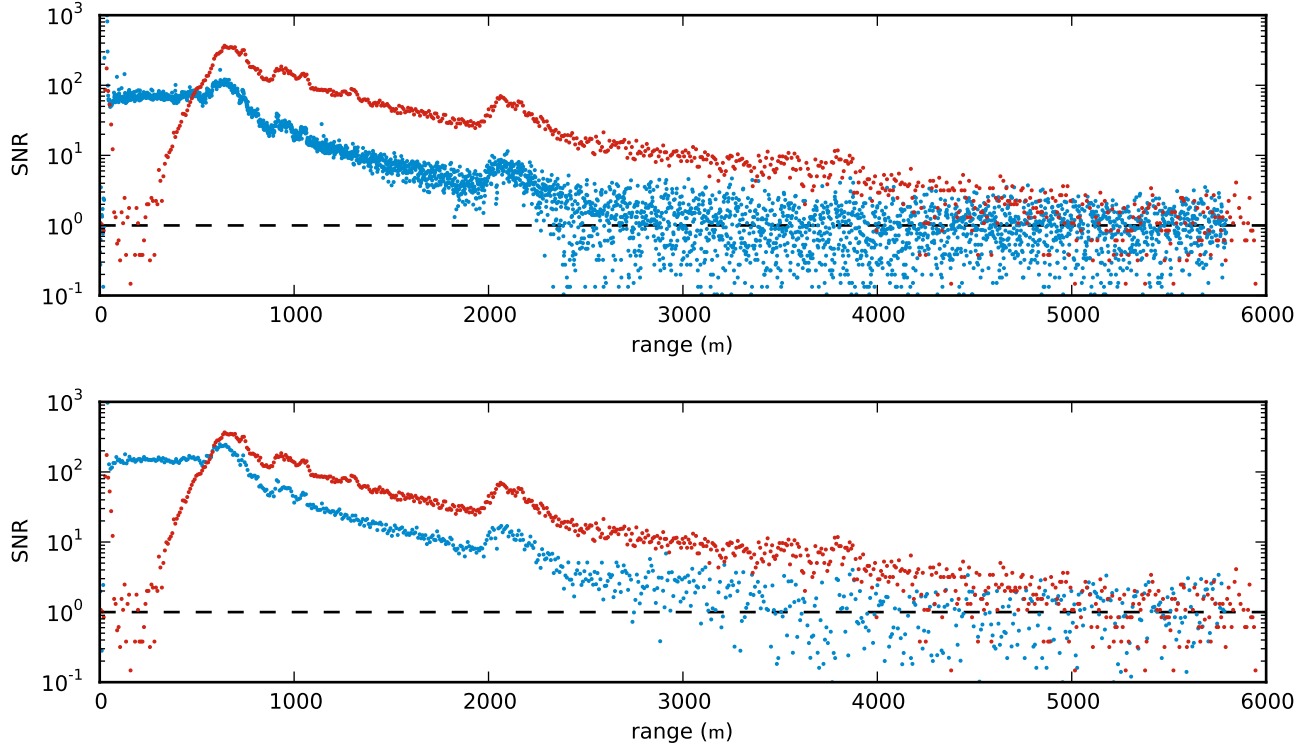


Figure 5: Comparison of raw SNR. Blue data points are the result of one pulse of the REAL and the red data points are the result of a 0.1 s integration of photon counts for the SAMPLE. Top panel is with the native REAL resolution (1.5 m range gate), bottom panel with a 5-point binning to match SAMPLE resolution.

large scale features from the images. The high-pass filter is applied along the radial direction. In this work, we used a 500 m window to remove radially-oriented features larger than 250 m. This corresponds to a 333-point filter for REAL and 67-point filter for SAMPLE. Backscatter data after applying these filters are shown in Figs. 6 and 7.

For the motion estimation algorithms to be successful, sufficient raw SNR is not the only requirement. In addition, the images must contain coherent aerosol features. There are times, typically during the night, when very few features are present within the scan domain, and other situations where features exist but are dominated by the random noise – especially in the far range. It is therefore important to detect the presence of aerosol features in order to discard irrelevant data. This is achieved using a quantity that we call “image-SNR” (iSNR).¹² iSNR is defined as the ratio of the local standard deviation of coherent signal $\sigma_I(r, \theta)$ to the local standard deviation of noise $\sigma_\epsilon(r, \theta)$. These local standard deviations are estimated from the autocorrelation function of the high-pass median filtered backscatter data, along the radial dimension (see Fig. 8). In this work, a window length of ≈ 280 m was used, that is 256 points for REAL and 32 points for SAMPLE data.

Coherent aerosol features correspond to larger values of iSNR. A simple thresholding can be applied to discriminate between features and irrelevant data – see an example of a scan by SAMPLE in Fig. 9. During this study, it was found that the low-pass median filter, applied to the backscatter along the radial direction in order to remove small hard-target outliers, has a deep influence on the iSNR. This is due to the fact that the low-pass median filter acts as a denoiser and thus increases the iSNR, as shown in Fig. 10. Without low-pass filtering, the iSNR from the SAMPLE is better than the REAL’s past 0.5–1 km (top row). A low-pass filtering of the backscatter using a 22 m window (15 points for the REAL, 3 points for SAMPLE) highly reduces the noise and increases REAL’s iSNR (bottom panel), in particular in the mid-range. A bump in the iSNR corresponding to an aerosol plume appears progressively between 3–4 km, while it was previously buried in the noise. A

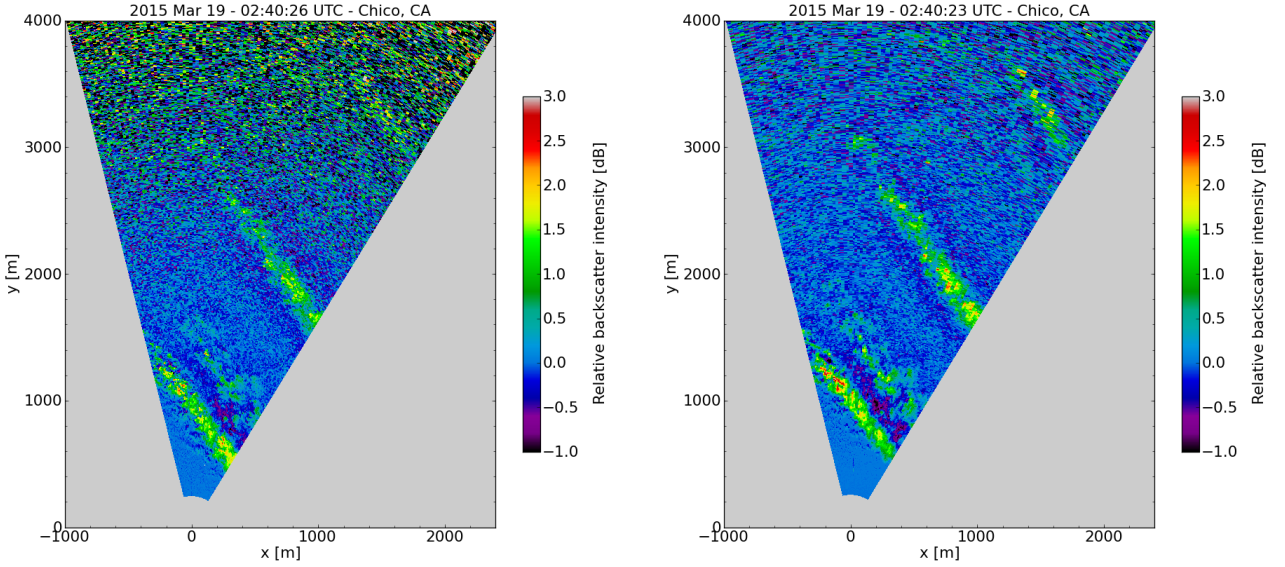


Figure 6: Left panel: One high-pass median filtered PPI scan from the REAL. Right panel: the same from the SAMPLE. No low-pass median filtering was applied.

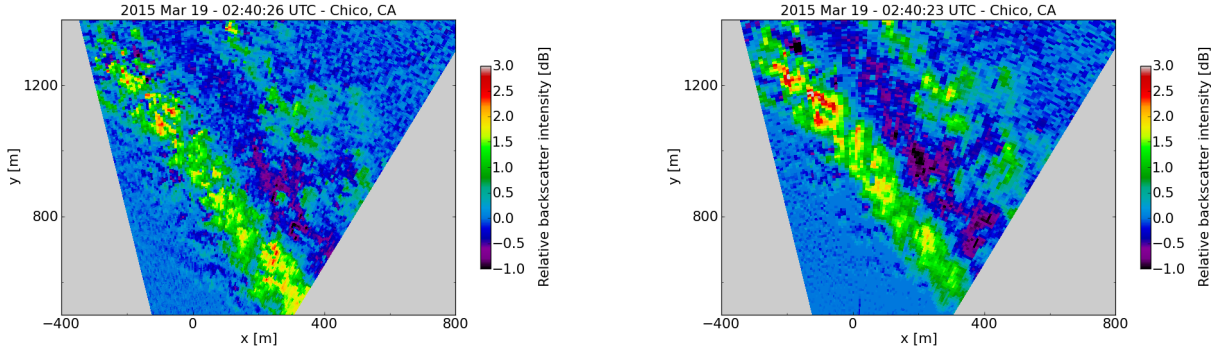


Figure 7: Left panel: Zoomed-in region from one high-pass median filtered PPI scan from the REAL. Right panel: the same from the SAMPLE.

direct consequence of this analysis is that the threshold value used to discriminate between coherent features and irrelevant data (Fig. 9) has to be adapted to the size of the low-pass filter.

While low-pass filtering can significantly denoise data from the REAL and increase the iSNR, it also destroys some of the fine-scale structures. Thus, a trade-off must be found between the amount of denoising and the scales to be preserved. A future study will examine how the low-pass filtering affects the wind motion estimation.

7. COMPARISON OF WIND DATA

The wind estimation was performed at the end of the experiment, on 18–20 March 2015. Both instruments performed 45° sector scans covering $[-15, 30]^\circ$ azimuth at 2° elevation in about 13 s for the REAL and 12 s for SAMPLE. Wind estimates were retrieved from both instruments using the two approaches that were previously validated on the REAL against an independent Doppler lidar: cross-correlation¹¹ and wavelet-based optical flow.¹²

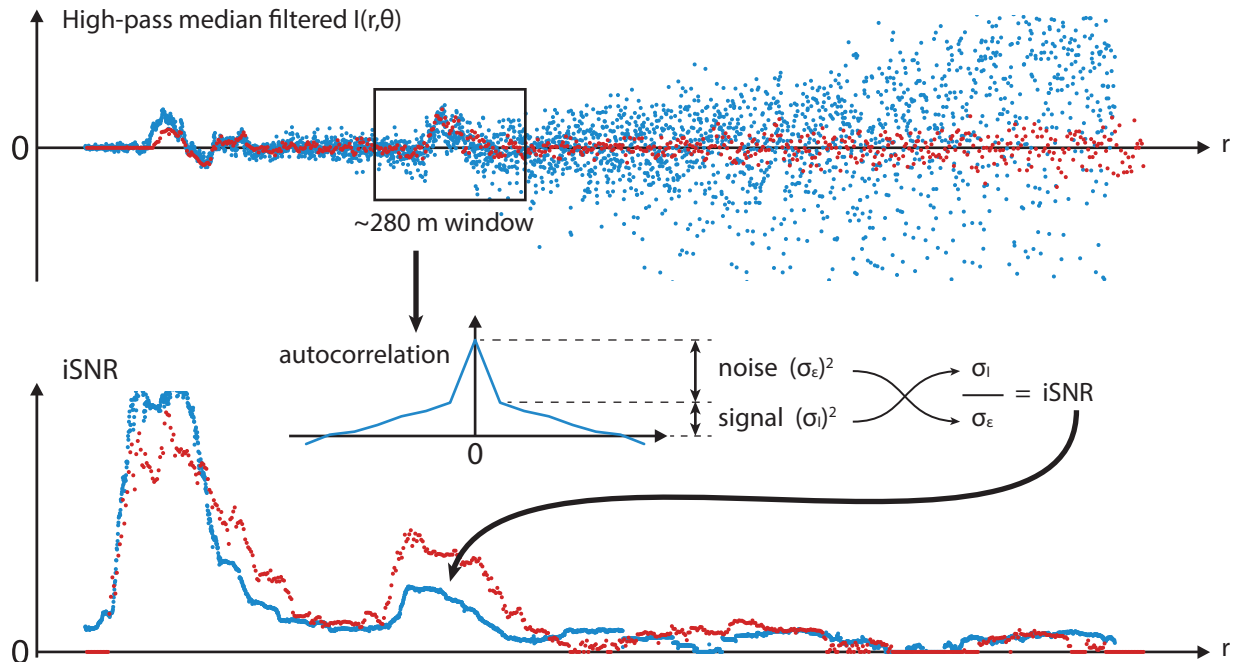


Figure 8: Diagram showing how image-SNR (“iSNR”) is calculated with actual data. Blue data points are from the REAL and red data points are from the SAMPLE. A gliding 280-m window (square on top graph) is applied to each high-pass median filtered radial array. Autocorrelation functions (middle sketch) and iSNR (bottom graph) are computed for all window positions.

At the time of the experiment, SAMPLE was not equipped with a “quick fly-back” strategy like the REAL, but rather swept continuously back and forth at the same rate. For the purpose of motion estimation, this has the disadvantage of having to skip every other scan in order to obtain the same time-step between two consecutive samples at any given location of the scan domain. Thus, the actual inter-scan time-step for SAMPLE data is 24 s. This limits our ability to compare directly REAL and SAMPLE estimates: since larger time-steps result in larger errors, the influence of the scan strategy cannot be separated from other parameters such as the radial resolution or sensitivity to noise.

Figure 11 shows an example of wind fields estimated by both instruments approximately at the same time. Each vector field is superimposed over the first scan of the pair used for the motion estimation. Both the aerosol features, in the background, and the vector fields look very similar. The lack of vectors in the very near range for SAMPLE (right panel) is explained by the slightly different masking strategies for each instrument (Sect. 6 and Fig. 9).

Figure 12 presents time-series of wind speed and direction measured on March 18 by both instruments using the wavelet-based optical flow algorithm, “Typhoon”. These values are extracted from the wind fields in a 50 m-radius area located at 1.5 km range and 15° azimuth. Except for a few spurious estimates, both series are in very good agreement. Figure 13 shows time-series measured on March 20 from SAMPLE data by both estimation methods. Values were extracted from the same location as with the series of Fig. 13. Again, both series are in very good agreement.

8. DISCUSSION AND CONCLUSION

While the raw SNR of the SAMPLE data may be greater than that of the untouched REAL data (Fig. 5), subjective visual inspection of the imagery (such as Fig. 7) suggest that the REAL reveals more fine-scale detail in the radial dimension. For some applications, such as observing microscale gravity waves,¹³ this detail is very

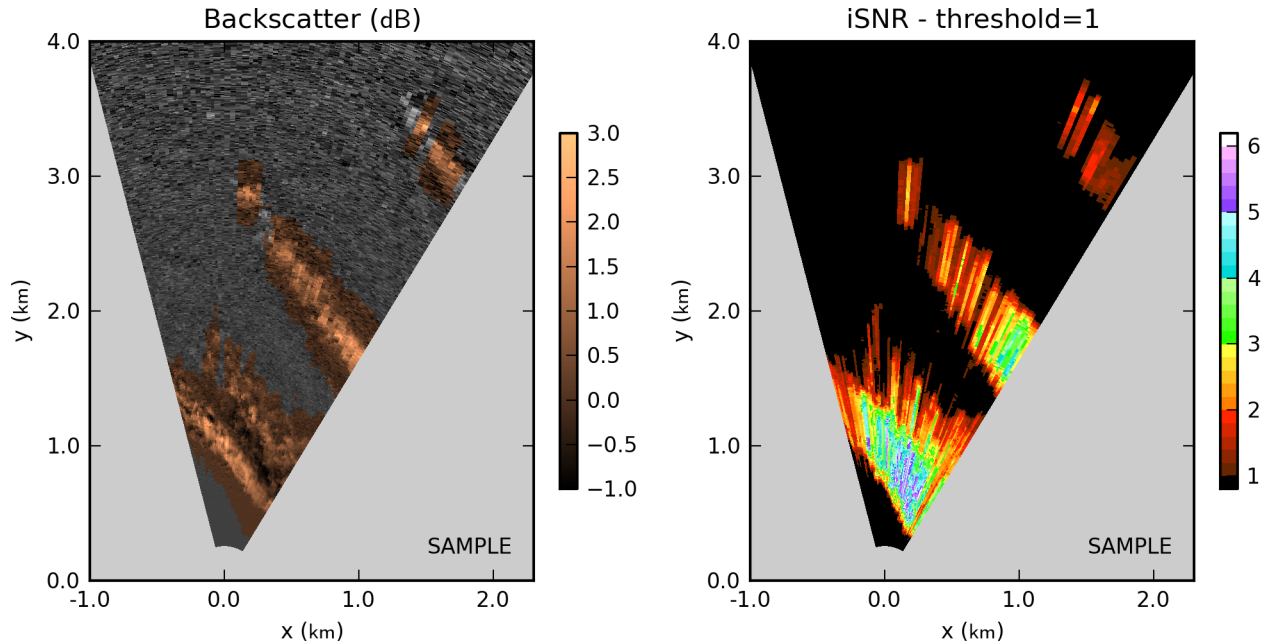


Figure 9: Example of iSNR-based masking of irrelevant data for a SAMPLE scan. The copper-colored aerosol features (left) correspond to an $iSNR > 1$ (right), while noisy and/or feature-less data is shown in gray shades.

valuable. However, for other applications, such as the estimation of wind fields, its value is questionable. This is because while the distance between samples in range remains constant with range, the distance between samples in the azimuthal direction increases with range. This fact is an unavoidable artifact of the polar coordinate system in which scanning lidar data are collected. Therefore, the high radial resolution of the REAL may be valuable to motion estimation in short ranges where the azimuthal resolution may be comparable to the radial resolution. However, at far ranges the detail is likely to be of no value in the motion estimation since there are no closely spaced neighboring arrays to sample that fine-scale structure in a subsequent scan.

The main conclusion of our experiment and analysis of data is that the size, weight, and complexity of the REAL appear to be avoidable in future designs and that a path exists for improved wind field measurements from a higher performance and dramatically more compact and efficient system. Currently, the major advantages of the REAL are: (1) continuous all-weather operation (due to the housing and beam steering unit); (2) immunity from second-trip echoes—which is significant when working in terrain and near clouds; (3) insensitivity to background radiation levels; and (4) high range resolution. The major disadvantages of the REAL are mostly due to the transmitter that results in high levels of required maintenance, power consumption, and waste heat generation. It also requires a large and stable operating environment. In addition, the small APD used in the REAL makes focusing the backscatter radiation a challenge.

The major advantages of the SAMPLE are: (1) deployed size (approximately 1.4 cubic meters) and weight (approximately 450 lbs or 204 kg) and (2) improved performance in terms of backscatter signal to noise ratio. A significant advantage of the SAMPLE also is the power consumption: only 850 W. The major disadvantage of the SAMPLE are the second trip echoes. The reduced range resolution from that of the REAL appears to be only a minor disadvantage. Scanner fly-back capability that was lacking for this experiment was quickly added and utilized in the immediately subsequent deployment of SAMPLE to the northern California coast near Eureka.¹⁴

In terms of future steps, first, we would like to develop and apply a theoretical model to facilitate comparison and prediction of the performance of either style system (macropulse versus micropulse). Such a model would enable us to assess the merits of various system design trades. For example, to reduce the susceptibility to second trip echoes on a micropulse system, the pulse repetition frequency could be reduced to 10 kHz. Doing so

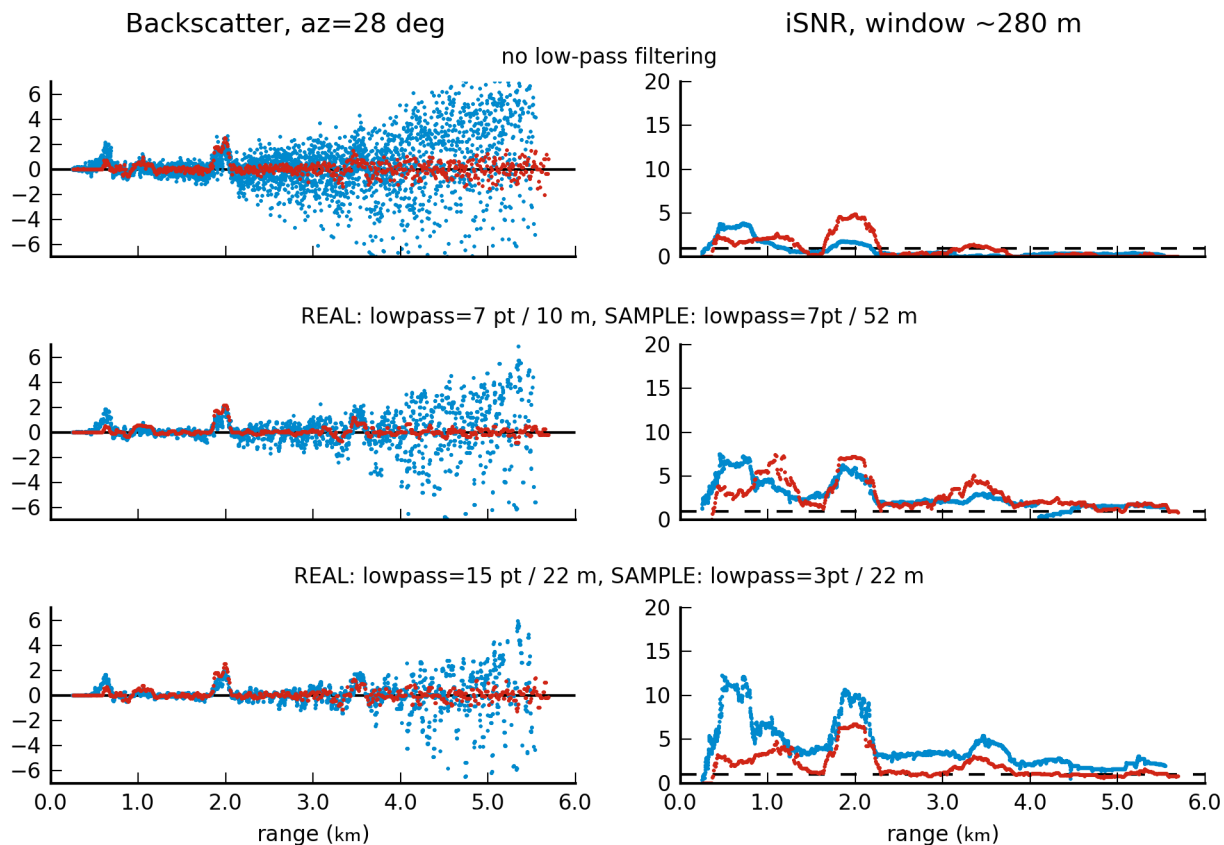


Figure 10: Effects of the low-pass filter on the backscatter (left) and iSNR (right) on a backscatter profile of REAL (red) and SAMPLE (blue) data. Low-pass filtering significantly reduces the noise on data from the REAL and increases the iSNR (bottom row), especially in the mid-range.

however would also reduce the average transmit power 66% of the current value. However, such a performance reduction might be compensated for by adding a temperature-controlled etalon to provide better rejection of background radiation. Use of larger diameter telescopes are another possibility to increase performance, but with larger collection area comes larger background radiation. Again, a model is needed to quantitatively assess the impact of the various design options. Second, the model would benefit from being validated by a long duration experiment whereby a SAMPLE and a REAL were operated for long periods (at least several months, preferably a year or more), under a wide variety of weather and background radiation conditions.

In terms of packaging, a shared telescope as described by Spuler et al.³ could eliminate the current biaxial design of SAMPLE and may result in an overall reduction in size, weight, and cost. In terms of configurations for enabling more atmospheric research, we expect greatly improved versatility from future designs. For example, a SAMPLE could easily be placed in a modest enclosure and pointed vertically to utilize the scanning capability of a roof-top beam steering unit and the protection of a secure, weatherproof enclosure. Such a configuration would enable continuous, long-term operations (i.e., experiment such as CHATS). However, the actual instrument could also be easily removed from the weatherproof enclosure and shipped for rapid deployments on various platforms.

ACKNOWLEDGMENTS

This work was supported by the National Science Foundation's Physical and Dynamic Meteorology Program under awards AGS 0924407 and 1228464. Deployment of the SAMPLE in Chico CA in March 2015 was supported by HDTRA2-15-C-0003.

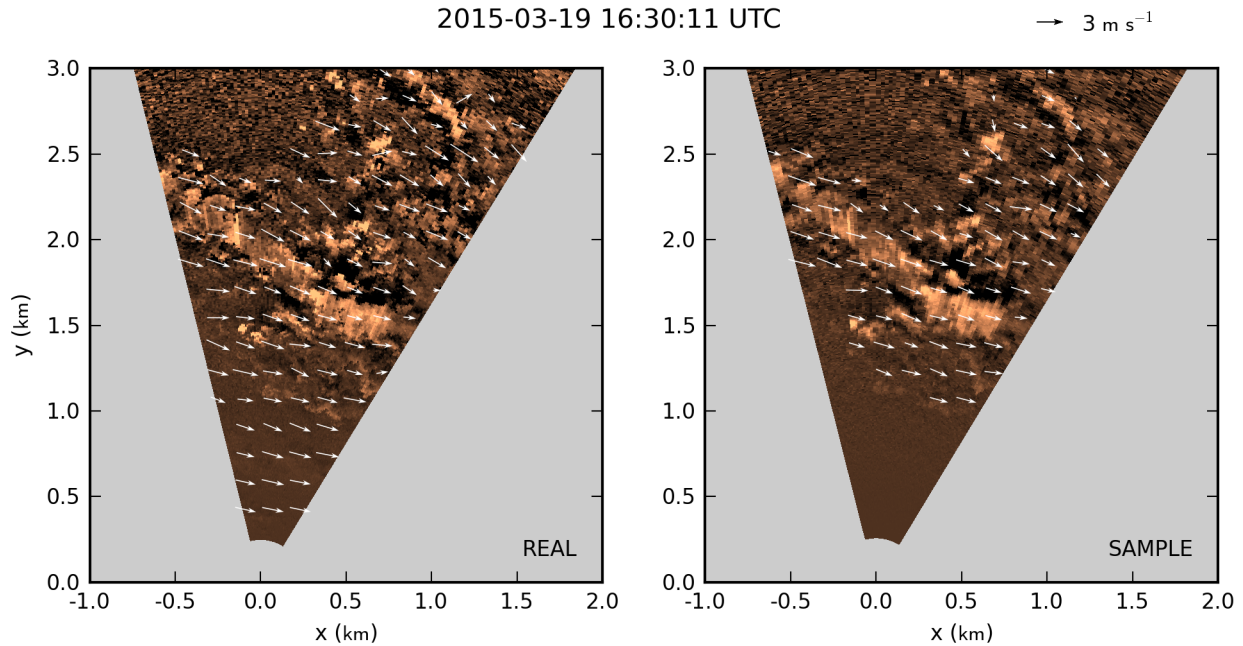


Figure 11: Example of wind fields estimated by the wavelet-based optical flow algorithm from REAL (left) and SAMPLE data (right). Wind speed is $\approx 3 \text{ m s}^{-1}$. Copper-colored background is the aerosol backscatter of the first scan of the pair used to retrieve each wind field. The density of wind field vectors shown was decimated by a factor of 20 in both dimensions for the sake of visualization.

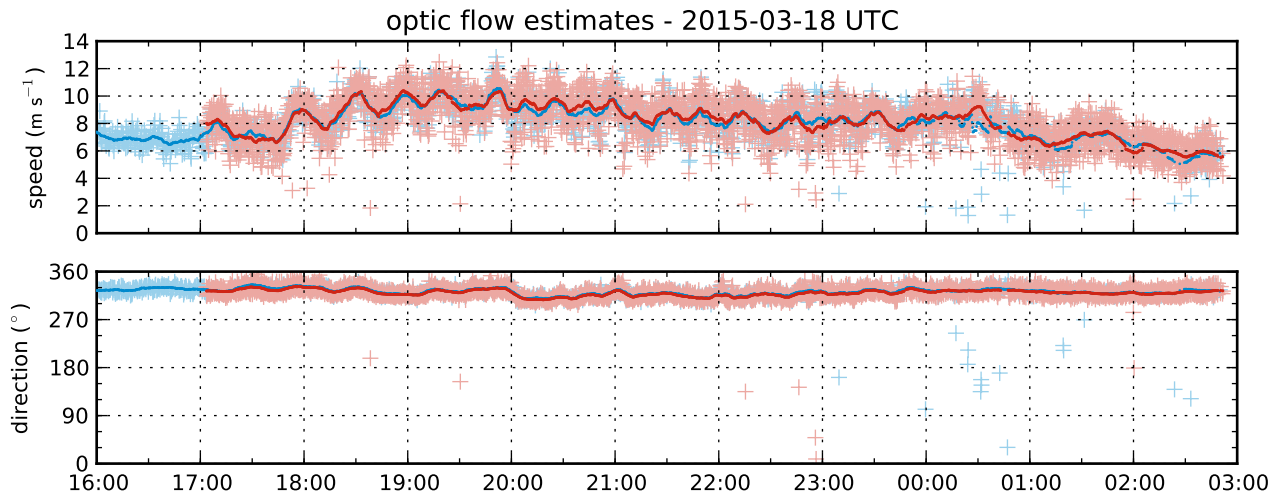


Figure 12: Comparison of wind speed (top) and direction (bottom) measured by the wavelet-based optical flow for a point at 1.5 km range, 15° azimuth from the instruments. Blue data points are from REAL and red data points are from SAMPLE. + markers are instantaneous measures and continuous lines are 10-min rolling averages.

REFERENCES

- [1] Zhang, Y., Yi, F., Kong, W., and Yi, Y., “Slope characterization in combining analog and photon count data from atmospheric lidar measurements,” *Appl. Opt.* **53**, 7312–7320 (Nov 2014).

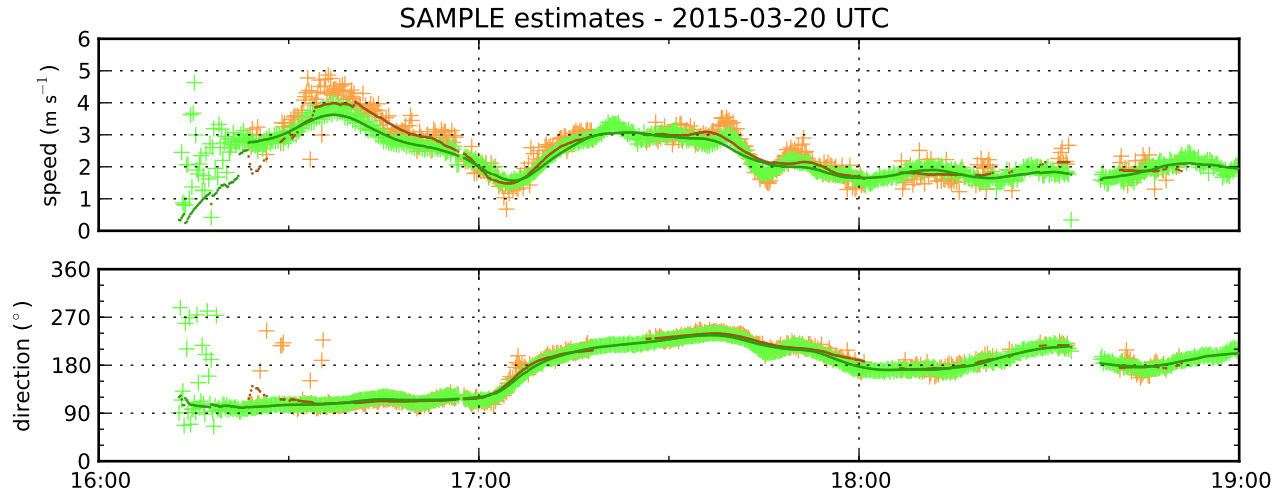


Figure 13: Comparison of wind speed (top) and direction (bottom) measured from SAMPLE data for a point at 1.5 km range, 15° azimuth from the instruments. Orange data points are from the wavelet-based optical flow and green data points are from the cross-correlation. + markers are instantaneous measures and continuous lines are 10-min rolling averages.

- [2] Razenkov, I., *Characterization of a Geiger-Mode Avalanche Photodiode Detector for High Special Resolution Lidar*, Master's thesis, University of Wisconsin - Madison, 1225 West Dayton Street, Madison, WI 53706 (2010).
- [3] Spuler, S. M., Repasky, K. S., Morley, B., Moen, D., Hayman, M., and Nehrir, A. R., "Field-deployable diode-laser-based differential absorption lidar (dial) for profiling water vapor," *Atmos. Meas. Tech.* **8**(3), 1073–1087 (2015).
- [4] Spinhirne, J. D., "Micro pulse lidar," *IEEE Trans. Geosci. Remote Sensing* **31**, 48–55 (1993).
- [5] Mayor, S. D. and Spuler, S. M., "Raman-shifted Eye-safe Aerosol Lidar," *Appl. Optics* **43**, 3915–3924 (2004).
- [6] Spuler, S. M. and Mayor, S. D., "Scanning eye-safe elastic backscatter lidar at 1.54 microns," *J. Atmos. Ocean. Technol.* **22**, 696–703 (2005).
- [7] Mayor, S. D., Spuler, S. M., Morley, B. M., and Loew, E., "Polarization lidar at 1.54-microns and observations of plumes from aerosol generators," *Opt. Eng.* **46**, DOI: 10.1117/12.781902 (2007).
- [8] Spuler, S. M. and Mayor, S. D., "Raman shifter optimized for lidar at 1.5-micron wavelength," *Appl. Optics* **46**, 2990–2995 (2007).
- [9] Mayor, S. D., Benda, P., Murata, C. E., and Danzig, R. J., "Lidars: A key component of urban biodefense," *Biosecur. Bioterror.* **6**, 45–56, DOI: 10.1089 bsp.2007.0053 (2008).
- [10] Mayor, S. D., Lowe, J. P., and Mauzey, C. F., "Two-component horizontal aerosol motion vectors in the atmospheric surface layer from a cross-correlation algorithm applied to scanning elastic backscatter lidar data," *J. Atmos. Ocean. Technol.* **29**, 1585–1602 (2012).
- [11] Hamada, M., Dérian, P., Mauzey, C. F., and Mayor, S. D., "Optimization of the cross-correlation algorithm for two-component wind field estimation from single aerosol lidar data and comparison with Doppler lidar," *Submitted to J. Atmos. Ocean. Technol.* (2015).
- [12] Dérian, P., Mauzey, C. F., and Mayor, S. D., "Wavelet-based optical flow for two-component wind field estimation from single aerosol lidar data," *J. Atmos. Ocean. Technol.* (In Press) (2015).
- [13] Randall, T. N., *Observations of microscale gravity waves in the nocturnal boundary layer above an orchard canopy by a horizontally scanning lidar*, Master's thesis, California State University Chico (May 2015).
- [14] Mayor, S. D., Dérian, P., Mauzey, C. F., and Hamada, M., "Two-component wind fields from single scanning aerosol lidar," SPIE (August 2015). Paper 9612-13.